Using wafer scale ferroelectric domains of $LiNbO_3$ to form permanent planar *p-n* junction in narrow band gap nanocrystals

Mariarosa Cavallo[1], Ankita Ram[2], Satakshi Pandey[2], Thomas Maroutian[3], Erwan Bossavit[4], Nicolas Ledos[1], Adrien Khalili[1], Huichen Zhang[1], Yoann Prado[1], Do Lam Nguyen[1,5], Tung Huu Dang[1], Hicham Majjad[2], Johan Biscaras[5], Jose Avila[4], Jean Francois Dayen[2,6], Emmanuel Lhuillier[1*], Debora Pierucci[1]

[1] Sorbonne Université, CNRS, Institut des NanoSciences de Paris, 75005 Paris, France.
[2] Université de Strasbourg, IPCMS-CNRS UMR 7504, 23 Rue du Loess, 67034 Strasbourg, France.
[3] Centre de Nanosciences et de Nanotechnologies, CNRS, Université Paris-Saclay, 10 boulevard Thomas Gobert, 91120 Palaiseau, France.
[4] Synchrotron SOLEIL, L'Orme des Merisiers, Départementale 128, 91190 Saint-Aubin, France.
[5]Sorbonne Université, Muséum National d'Histoire Naturelle, UMR CNRS 7590, Institut de Minéralogie, de Physique des Matériaux et de Cosmochimie, IMPMC, 75005 Paris, France.
[6]Institut Universitaire de France, 1 rue Descartes, 75005 Paris, France.

*To whom correspondence should be sent: el@insp.upmc.fr

Abstract: *p-n* junctions based on nanocrystals (NCs) now serve as fundamental components in optoelectronics. However, the process of designing these *p-n* junctions has largely relied on empirical choices, either for ligand exchange or for the selection of charge transport layers. Thus, a systematic strategy is still lacking. In this study, we explore the utilization of ferroelectric domains as a general method for remotely inducing the formation of a *p-n* junction. To ensure compatibility with devices of various designs, we employ a commercially available periodically poled $LiNbO_3$ (PPLN) substrate commonly used in non-linear optics. We engineer a PPLN/graphene/HgTe heterostructure and demonstrate its planar photodiode behavior. Through X-ray photoemission microscopy, we confirm that the rectifying behavior stems from the influence of the ferroelectric domains, by ruling out the possibility of the formation of non-ohmic contacts at the electrode/semiconductor interfaces. This approach proves to be quite general and holds promise for the future design of high-speed nanocrystal-based photodiodes.

Keywords: ferroelectric, nanocrystals, infrared, *p-n* junction

As the use of nanocrystals (NCs) expands, they transition from optically active material to a viable building block for optoelectronic applications.[1] where both spectral and electrical properties have central roles. The design of fundamental building blocks, such as *p-n* junctions, becomes increasingly critical. Such basic components are used for light emitting diodes as well as for light sensors design. However, a general strategy for obtaining a control of the carrier density landscape[2–5] in nanocrystals is still lacking.

The most established procedure to tune the doping of nanocrystals relies on ligand exchange.[6–8] During this process, the dipoles associated with the capping molecules induce band bending, the direction of which affects the relative position of the band with respect to the Fermi level, resulting in a net change in carrier density. However, this strategy depends on the material, on the exposed facets, and on the NC size, therefore relying on an empirical approach. An alternative method to shape the carrier density landscape relies on gate control. The use of a dual gate has been proven to induce a planar *p-n* junction.[9–13] However, the phototransistor approach also introduces challenges, especially with the continuous application of bias, which leads to increased electrical consumption. Additionally, gate electrodes may introduce extra electrical noise into the system, which is highly problematic for infrared sensing that inherently suffers from limited signal to noise ratio due to thermal activation of carrier Consequently, coupling to a static field appears more promising. A substantial static electric field can be generated through ferroelectric materials. However, this concept has been predominantly explored in the realm of 2D materials,[14–17] with minimal attention given to the case of nanocrystals. In fact, ferroelectric gates have primarily been employed in the paraelectric regime, functioning as high-*k* materials and capitalizing on the divergence of the dielectric constant when the material operates near the Curie temperature. This phenomenon[18] has been observed in ferroelectric polymers[19] and oxide layers.[20] Previously, Cavallo *et al.*,[21] have reported utilizing the remnant polarization from ferroelectrics to exert control over the NC carrier density. In their study, a $PbZrTiO_3$ (PZT) layer was utilized as the ferroelectric material, and its orientation was defined using piezoresponse force microscopy (PFM). However, since this approach relies on near-field probes, it has the notable limitation of being restricted to small device areas (a few hundred μm^2). This necessitates exploring alternatives to accelerate production and potentially design more than a single element simultaneously.

Manufactured $LiNbO_3$ substrates with controlled polarization are extensively utilized in nonlinear optics. Periodically poled $LiNbO_3$ (PPLN) is employed to achieve quasi-phase matching conditions and is readily available in large-scale format substrates. However, in our research, we deviate from the conventional use of PPLN. Instead, we employ it as a strategy to create *p-n* junctions in an array of narrow-bandgap nanocrystals that exhibit optical activity in the mid-wave infrared region (3-5 µm range). In our study, we demonstrate the capability to form *p-n* junctions using this innovative approach. Furthermore, we showcase its effectiveness for mid-infrared sensing applications.

We begin the process by designing electrodes on an insulating PPLN substrate, made of full-wafer arrays of alternating ferroelectric domains of opposite polarities, with a 600 µm periodicity. To create a *p-n* junction, two electrodes are placed on two consecutive ferroelectric domains. To harness the remnant electric field generated by the substrate effectively, we employ large-scale graphene electrodes deposited by chemical vapor deposition (CVD).[22,23] This allows the stray electric field from the ferroelectric substrate not only to influence the channel between the electrodes but also over the electrodes themselves thanks to the partial transparency of graphene to the electric field. Compared to gold electrodes (Figure S2), this favors the diode behavior and leads to stronger rectifying ratio. A comprehensive description of the fabrication procedure can be found in the supplementary methods section; see Figure S1. In summary, CVD graphene is first transferred onto

the PPLN substrate. Subsequently, the graphene layer is etched to form the electrodes, and a lithography step is employed to define metallic contacts away from the ferroelectric interface. **Figure 1**a provides a schematic representation of the device, while an optical microscope image of the fabricated device is presented in **Figure 1**b.

Raman spectroscopy conducted on the functionalized substrate can be used to locate the graphene electrodes and verify the completeness of the etching. On the pristine substrate, the Raman spectrum (**Figure 1**c-d) predominantly exhibits the 2E mode from $LiNbO_3$. On the electrodes, additional features associated with the G mode and the 2D mode of graphene become apparent. An intensity map relative to the energy of the G mode is depicted in **Figure 1**c, indicating the absence of graphene within the device's channel which confirms it is completely etched.

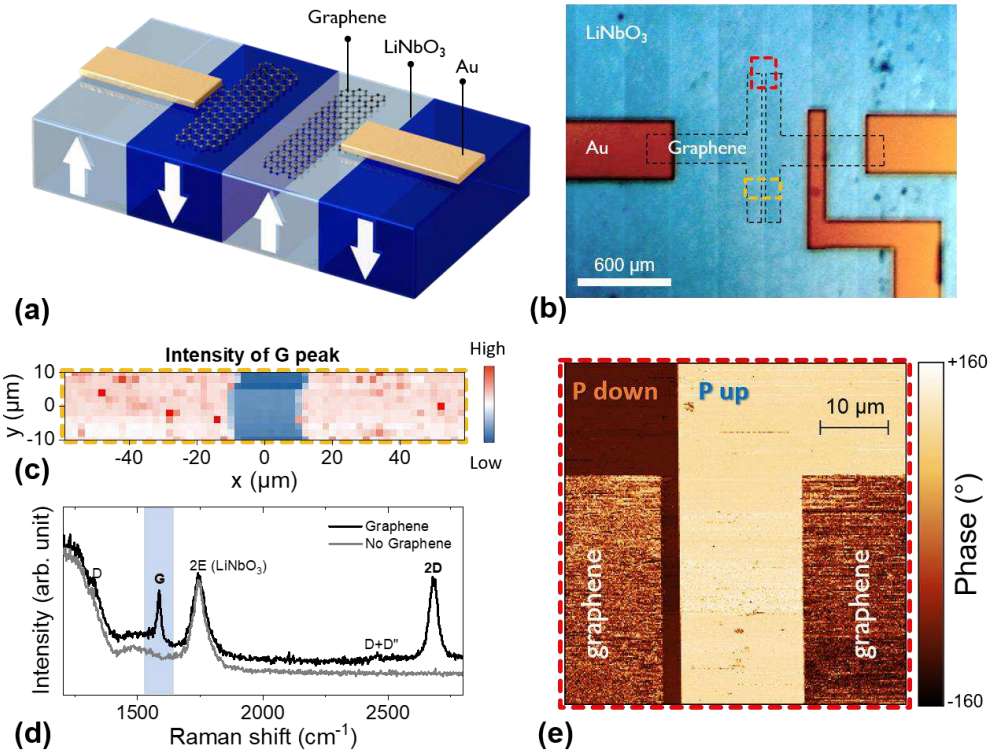

Figure 1 Graphene electrode on PPLN. *a. Schematic of PPLN substrate functionalized by graphene electrodes. b. Optical microscopy of PPLN substrate functionalized by graphene electrodes. The area corresponding to graphene is highlighted with black dashed line. c. Raman map of the graphene G peak over the area highlighted in yellow in part b. d. Raman spectra over the PPLN substrate and over graphene functionalized PPLN. e. PFM image of the area highlighted in red in part b, showing that the two graphene electrodes are fabricated over domain of opposite polarities.*

We subsequently employed PFM to determine the polarity of the $LiNbO_3$ beneath each graphene electrode, as shown in **Figure 1**e and Figure S3-4. The strong contrast due to 180° phase change in the phase imaging confirmed their opposite polarities.

We then coupled this device to a material sensitive to the mid-infrared. HgTe nanocrystals (NCs) were grown using the procedure developed by Keuleyan *et al.*[24] Their size, approximately 10 nm as observed in electron microscopy (see **Figure 2**b), was chosen to yield absorption spectra with a cut-off around 3000 cm^{-1} (≈3.3 µm) at room temperature (**Figure 2**a), which then redshifted upon cooling.[25] The HgTe NCs were ligand-exchanged to form an ink,[26,27] wherein the resulting thin passivation shell later facilitates interparticle electronic coupling and improves conduction in the film. This ink was spin-coated onto the graphene-functionalized PPLN substrate.

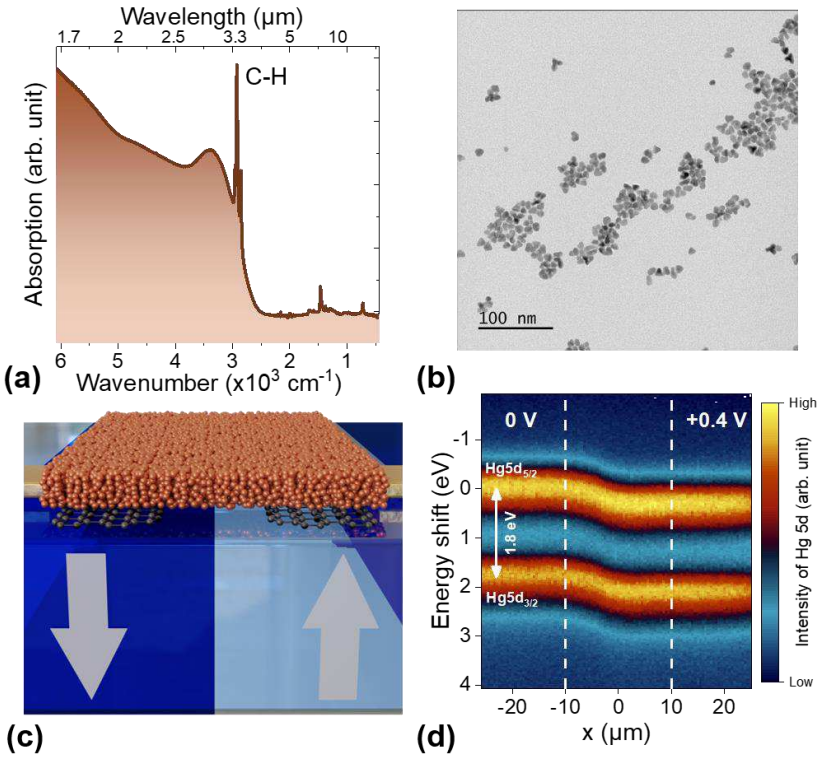

***Figure 2 HgTe NC sensitized graphene electrodes**. a. Absorption spectrum from the HgTe NCs used to sensitize the graphene electrodes to the infrared. b. TEM image of the HgTe NCs. c. Schematic of the final device where the HgTe NC film is bridging the graphene electrodes over two ferroelectric domains with opposite polarities. d. Energy shift over the device, measured at 180 K by the shift of the Hg 5d state, while 0.4 V bias is applied. The white lines show the position of the two electrodes.*

In order to assess the ability of the graphene layer to function as a proper electrode (*i.e.,* able to apply bias) and to determine the nature of the electrode/semiconductor interface (*i.e.*, ohmic contact or rectifying contact), we used soft X-ray photoemission microscopy[21,28–30]. This method has been

proven reliable to map out *operando* a device's energy landscape. A synchrotron beam at 95 eV was focused on the sample using a Fresnel zone plate, resulting in a 700 nm spot size on the sample. The sample was then scanned point by point in the *xy* plane, and for each point we collected a photoemission spectrum (see Figure S5). We tracked the Hg 5d state (Figure S6) which has a low binding energy (binding energy = 8 eV) compatible with the chromatic window of the focusing zone plate. This state presents a doublet (Hg $5d_{5/2}$ and Hg $5d_{3/2}$) with a 1.8 eV spin-orbit splitting. **Figure 2**d displays the energy of this state as a function of position, while a bias of 0.4 V was applied. We observe a similar shift in binding energy across the channel. Within the spatial resolution of the experiment, the energy drop appears continuous and quasi-linear, suggesting that the HgTe-graphene interface leads to the formation of an ohmic contact. Thus, we can exclude the possibility that any observed diode-like behavior could be the result of rectifying contacts.

We then proceeded to measure the transport properties of the device. Close to room temperature, the IV curve remains predominantly linear and symmetrical, as depicted in **Figure 3**a. One may wonder if the ferroelectric polarization is only emerging at low temperature. However, in the case of $LiNbO_3$[31–33] the Curie temperature is very high (1480 K) compared to the relevant range of operating temperature for mid-infrared sensors (100-300 K), and the polarization of the material appears almost constant in this temperature range[34]. In fact, the absence of diode behavior is rather an inherent characteristic of narrow band gap NCs. A similar behavior is observed in all mid-wave infrared diodes[35,36] based on HgTe NCs with a vertical geometry (Figure S7) and even in dual-gated (using Al_2O_3 as dielectric) field effect transistor (Figure S8). In this narrow band gap semiconductor, the thermally activated carrier density is high and competes with the gate/ferroelectric induced carrier density: as temperature is reduced, electrical properties are no longer driven by thermally activated carriers and a diode behavior can be observed. Thus, once the device is cooled, the IV curve becomes strongly rectifying, exhibiting a current asymmetry exceeding 100. Since we have established the absence of rectifying contacts, this confirms the ability of the ferroelectric domains to remotely induce a *p-n* junction.

During forward operation under positive bias, it was observed that the downward polarization corresponds to an induced *n*-type behavior in HgTe, whereas the upward polarization leads to p-type behavior. This behavior mimics what has been observed in the case of HgTe coupled to PZT.[21] Interestingly, this contrasts with the trend observed in most 2D transition metal dichalcogenides, where an upward polarization is generally associated with a *n*-type behavior. Furthermore, we verified that if the device is constructed on reverse polarization domains (upward and then downward, see Figure S3), the polarity of the device is reversed, as illustrated in **Figure 4**a. This confirms that for such nanocrystals, there is an intermediate dipole at play between the ferroelectric polarization and the NCs.

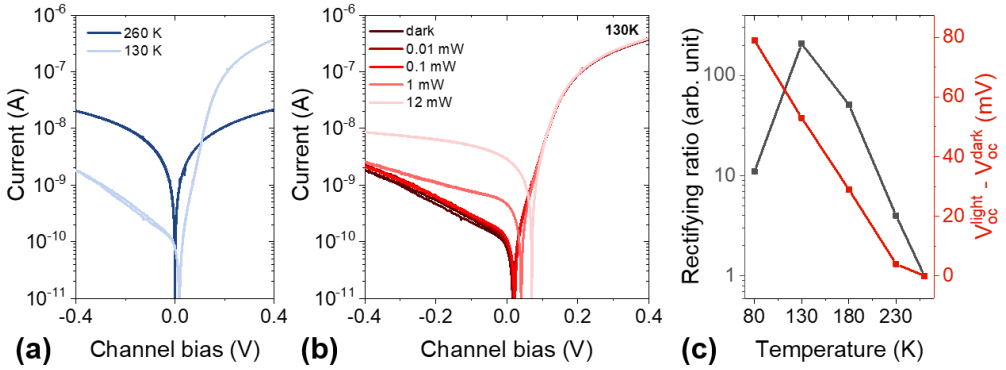

Figure 3 Electrical evidence for the formation of a p-n junction*. a. IV curves of the device depicted in* ***Figure 2*** *at low temperature and close to room temperature. b. IV curves under various irradiance at 1.55 µm. c. Rectifying ratio (defined as the ratio of the current under positive and negative bias at 0.4 V) and open circuit voltage under laser illumination (λ=1.55 µm at 12 mW) as a function of the device temperature.*

We then investigated the device's response to light. Upon illumination, we observe a clear triggering of open-circuit voltages and short-circuit photocurrents. Note that already in the dark there is a small non-null current under no bias, which we attribute to residual light flux and which shows that the device operates under background limited operation (BLIP). The strongest rectifying behavior is obtained for operation at 130 K, where the open circuit voltage reaches 80 mV, a value on par with state-of-the-art mid-IR HgTe vertical geometry diodes operated at the same temperature.[36,37] Such temperature is compatible with the high operating temperature (HOT) for mid-wave infrared devices. By following the slope (SS) of the IV curve (≈45 mV/decade at 130 K), we can extract the ideality factor (n_{id}) of the diode through the equation SS = ($n_{id}$$k_B$T/e).log(10) where k_B is the Boltzmann constant and *e* the elementary charge. We obtain a value n_{id}=1.8 close to two, indicating the predominance of the recombination current[38] over the diffusion current (for both carrier types). For this particle size, the Fermi level has been found from photoemission[39] to be quite deep in the band gap, which has been confirmed by transistor[40] measurements showing an ambipolar character for the transfer curve. This suggests the presence of a depleted junction at the *p-n* interface.

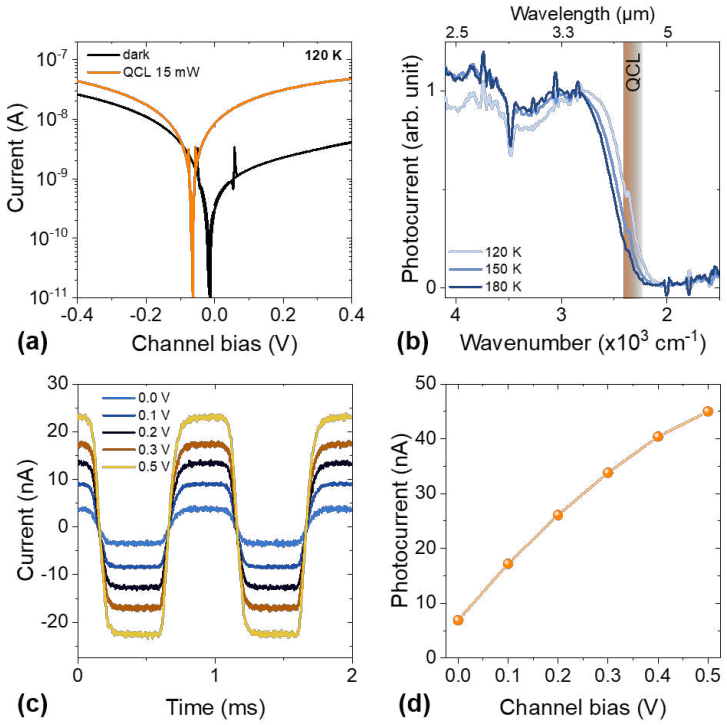

Figure 4 Photoresponse of the p-n junction. *a. IV curves under dark condition and under illumination by a QCL at 2200 cm^{-1} (4.4 µm, power 15 mW), at 120 K. This device is built so that the polarity of the two domains is opposite compared to the device used in Figure 3. This leads to inverted operation for the p-n junction, further confirming that the result is substrate induced. b. Photocurrent spectra at 0 V acquired at various temperatures. c. Time-resolved photocurrent signal (at 120 K) under illumination by a 4.4 µm QCL, optically chopped at 1 kHz, as reverse bias is increased. d. Photocurrent values, extracted from part c, as a function of bias.*

Finally, we have tested the potential of this ferroelectric-induced *p-n* junction for mid infrared sensing. The sample is illuminated by a quantum cascade laser (QCL), which matches the cut-off wavelength of the detector operated below 200 K, see **Figure 4**b. Though photons are less energetic than before at 1.55 µm, an open circuit voltage is still observed in the IV curve (**Figure 4**a). When no bias is applied, the responsivity of the device is rather limited at around 8 µA.W^{-1}, which reflects the fact that the device is too thin to absorb efficiently the light and also that the used QCL is only on the edge of the photoresponse. Absorption can easily be improved through the introduction of light management strategies.[20,41] Alternatively, the application of bias can also be used to increase the photocurrent magnitude, see **Figure 4**c-d. A moderate bias of 0.5 V enables a five-fold increase in the photosignal.

In summary, we have demonstrated the coupling of an infrared nanocrystal film with a full-wafer structured ferroelectric PPLN substrate, presenting a generic strategy for forming large-scale planar *p-n* junctions. One of the key advantages of this method is that it eliminates the need to identify multiple surface chemistries or meticulously choose appropriate charge-selective transport layers.

To confirm the origin of the rectification behavior in the IV curve, X-ray Photoemission microscopy was employed, ensuring that the rectification arises from the ferroelectric domains interface and not from possible Schottky interfaces with the electrode. This research holds great promise for the development of low-energy-consumption, high-speed photodiodes based on nanocrystals. Moreover, the proof-of-concept results demonstrate the potential of this strategy for energy harvesting, and could be extended in principle to any other quantum dots with band energy matching the solar spectrum. Future efforts will be directed towards integrating the concept of ferroelectric-induced remote doping with light resonators within a single structure.

Supplementary Material

Supplementary material include (*i*) procedure for nanocrystal growth, (*ii*) procedure for device fabrication, (*iii*) material characterization method and additional measurement with focus on PFM and XPS, (*iv*) additional electrical characterization.

ACKNOWLEDEGMENTS

The project is supported by ERC grants blackQD (grant n° 756225) and AQDtive (grant n°101086358). This work was supported by French state funds managed by the Agence Nationale de la recherche (ANR) through the grant Copin (ANR-19-CE24-0022), Frontal (ANR-19-CE09-0017), Graskop (ANR-19-CE09-0026), NITQuantum (ANR-20-ASTR-0008), Bright (ANR-21-CE24-0012), MixDFerro (ANR-21-CE09-0029), Quicktera (ANR-22-CE09-0018), Operatwist (ANR-22-CE09-0037-01) and E-map (ANR-23-CE). This project has received financial support from the CNRS through the MITI interdisciplinary programs (project within) and from the French national network RENATECH for nanofabrication. J.F.D thanks Institut Universitaire de France for financial support through Junior Chaire Grant.

CONFLICT OF INTEREST

The authors declare no competing interest.

REFERENCES

[1] M. Liu, N. Yazdani, M. Yarema, M. Jansen, V. Wood, and E.H. Sargent, Nature Electronics **4**, 548–558 (2021).
[2] S.C. Erwin, L. Zu, M.I. Haftel, A.L. Efros, T.A. Kennedy, and D.J. Norris, Nature **436**, 91–94 (2005).
[3] D. Yu, C. Wang, and P. Guyot-Sionnest, Science **300**, 1277–1280 (2003).
[4] A. Sahu, M.S. Kang, A. Kompch, C. Notthoff, A.W. Wills, D. Deng, M. Winterer, C.D. Frisbie, and D.J. Norris, Nano Lett. **12**, 2587–2594 (2012).
[5] M. Dufour, E. Izquierdo, C. Livache, B. Martinez, M.G. Silly, T. Pons, E. Lhuillier, C. Delerue, and S. Ithurria, ACS Appl. Mater. Interfaces **11**, 10128–10134 (2019).
[6] A. Chu, B. Martinez, S. Ferré, V. Noguier, C. Gréboval, C. Livache, J. Qu, Y. Prado, N. Casaretto, N. Goubet, H. Cruguel, L. Dudy, M.G. Silly, G. Vincent, and E. Lhuillier, ACS Appl. Mater. Interfaces **11**, 33116–33123 (2019).
[7] P.R. Brown, D. Kim, R.R. Lunt, N. Zhao, M.G. Bawendi, J.C. Grossman, and V. Bulović, ACS Nano **8**, 5863–5872 (2014).
[8] A. Robin, C. Livache, S. Ithurria, E. Lacaze, B. Dubertret, and E. Lhuillier, ACS Appl. Mater. Interfaces **8**, 27122–27128 (2016).
[9] S.-S. Chee, C. Gréboval, D.V. Magalhaes, J. Ramade, A. Chu, J. Qu, P. Rastogi, A. Khalili, T.H. Dang, C. Dabard, Y. Prado, G. Patriarche, J. Chaste, M. Rosticher, S. Bals, C. Delerue, and E. Lhuillier, Nano Lett. **21**, 4145–4151 (2021).

[10] C. Gréboval, C. Dabard, N. Konstantinov, M. Cavallo, S.-S. Chee, A. Chu, T.H. Dang, A. Khalili, E. Izquierdo, Y. Prado, H. Majjad, X.Z. Xu, J.-F. Dayen, and E. Lhuillier, ACS Appl. Electron. Mater. **3**, 4681–4688 (2021).
[11] T. Qin, G. Mu, P. Zhao, Y. Tan, Y. Liu, S. Zhang, Y. Luo, Q. Hao, M. Chen, and X. Tang, Science Advances **9**, eadg7827 (2023).
[12] S.Z. Bisri, C. Piliego, J. Gao, and M.A. Loi, Advanced Materials **26**, 1176–1199 (2014).
[13] S.Z. Bisri, S. Shimizu, M. Nakano, and Y. Iwasa, Advanced Materials **29**, 1607054 (2017).
[14] J.-W. Chen, S.-T. Lo, S.-C. Ho, S.-S. Wong, T.-H.-Y. Vu, X.-Q. Zhang, Y.-D. Liu, Y.-Y. Chiou, Y.-X. Chen, J.-C. Yang, Y.-C. Chen, Y.-H. Chu, Y.-H. Lee, C.-J. Chung, T.-M. Chen, C.-H. Chen, and C.-L. Wu, Nat Commun **9**, 3143 (2018).
[15] S. Wu, Y. Chen, X. Wang, H. Jiao, Q. Zhao, X. Huang, X. Tai, Y. Zhou, H. Chen, X. Wang, S. Huang, H. Yan, T. Lin, H. Shen, W. Hu, X. Meng, J. Chu, and J. Wang, Nat Commun **13**, 3198 (2022).
[16] L. Lv, F. Zhuge, F. Xie, X. Xiong, Q. Zhang, N. Zhang, Y. Huang, and T. Zhai, Nat Commun **10**, 3331 (2019).
[17] M. Soliman, K. Maity, A. Gloppe, A. Mahmoudi, A. Ouerghi, B. Doudin, B. Kundys, and J.-F. Dayen, ACS Appl. Mater. Interfaces **15**, 15732–15744 (2023).
[18] A.I. Khan, A. Keshavarzi, and S. Datta, Nat Electron **3**, 588–597 (2020).
[19] A.G. Shulga, L. Piveteau, S.Z. Bisri, M.V. Kovalenko, and M.A. Loi, Advanced Electronic Materials **2**, 1500467 (2016).
[20] C. Gréboval, A. Chu, D.V. Magalhaes, J. Ramade, J. Qu, P. Rastogi, A. Khalili, S.-S. Chee, H. Aubin, G. Vincent, S. Bals, C. Delerue, and E. Lhuillier, ACS Photonics **8**, 259–268 (2021).
[21] M. Cavallo, E. Bossavit, S. Matzen, T. Maroutian, R. Alchaar, T.H. Dang, A. Khalili, C. Dabard, H. Zhang, Y. Prado, C. Abadie, J.K. Utterback, J.F. Dayen, M.G. Silly, P. Dudin, J. Avila, E. Lhuillier, and D. Pierucci, Adv Funct Materials **33**, 2300846 (2023).
[22] H. Mishra, J. Panda, M. Ramu, T. Sarkar, J.-F. Dayen, D. Belotcerkovtceva, and M.V. Kamalakar, J. Phys. Mater. **4**, 042007 (2021).
[23] C. Gréboval, U.N. Noumbé, A. Chu, Y. Prado, A. Khalili, C. Dabard, T.H. Dang, S. Colis, J. Chaste, A. Ouerghi, J.-F. Dayen, and E. Lhuillier, Appl. Phys. Lett. **117**, 251104 (2020).
[24] S. Keuleyan, E. Lhuillier, and P. Guyot-Sionnest, J. Am. Chem. Soc. **133**, 16422–16424 (2011).
[25] N. Moghaddam, C. Gréboval, J. Qu, A. Chu, P. Rastogi, C. Livache, A. Khalili, X.Z. Xu, B. Baptiste, S. Klotz, G. Fishman, F. Capitani, S. Ithurria, S. Sauvage, and E. Lhuillier, J. Phys. Chem. C **124**, 23460–23468 (2020).
[26] B. Martinez, J. Ramade, C. Livache, N. Goubet, A. Chu, C. Gréboval, J. Qu, W.L. Watkins, L. Becerra, E. Dandeu, J.L. Fave, C. Méthivier, E. Lacaze, and E. Lhuillier, Advanced Optical Materials **7**, 1900348 (2019).
[27] X. Lan, M. Chen, M.H. Hudson, V. Kamysbayev, Y. Wang, P. Guyot-Sionnest, and D.V. Talapin, Nat. Mater. **19**, 323–329 (2020).
[28] M. Cavallo, E. Bossavit, H. Zhang, C. Dabard, T.H. Dang, A. Khalili, C. Abadie, R. Alchaar, D. Mastrippolito, Y. Prado, L. Becerra, M. Rosticher, M.G. Silly, J.K. Utterback, S. Ithurria, J. Avila, D. Pierucci, and E. Lhuillier, Nano Lett. **23**, 1363–1370 (2023).
[29] M. Cavallo, R. Alchaar, E. Bossavit, H. Zhang, T.H. Dang, A. Khalili, Y. Prado, M.G. Silly, J.K. Utterback, S. Ithurria, P. Dudin, J. Avila, D. Pierucci, and E. Lhuillier, Nanoscale **15**, 9440–9448 (2023).
[30] A. Khalili, M. Cavallo, E. Bossavit, R. Alchaar, T.H. Dang, C. Dabard, H. Zhang, N. Ledos, V. Parahyba, P. Potet, J.K. Utterback, Y. Prado, M.G. Silly, P. Dudin, J. Avila, D. Pierucci, and E. Lhuillier, ACS Appl. Electron. Mater. **5**, 4377–4384 (2023).
[31] T. Weigel, C. Ludt, T. Leisegang, E. Mehner, S. Jachalke, H. Stöcker, T. Doert, D.C. Meyer, and M. Zschornak, Phys. Rev. B **108**, 054105 (2023).
[32] S.L. Bravina, A.N. Morozovska, N.V. Morozovsky, and Y.A. Skryshevsky, Ferroelectrics **298**, 31–42 (2004).

[33] S.L. Bravina, N.V. Morozovsky, A.N. Morozovska, S. Gille, J.-P. Salvestrini, and M. Fontana, Ferroelectrics **353**, 636–645 (2007).
[34] Q. Peng, and R.E. Cohen, Phys. Rev. B **83**, 220103 (2011).
[35] M.M. Ackerman, X. Tang, and P. Guyot-Sionnest, ACS Nano **12**, 7264–7271 (2018).
[36] T.H. Dang, M. Cavallo, A. Khalili, C. Dabard, E. Bossavit, H. Zhang, N. Ledos, Y. Prado, X. Lafosse, C. Abadie, D. Gacemi, S. Ithurria, G. Vincent, Y. Todorov, C. Sirtori, A. Vasanelli, and E. Lhuillier, Nano Lett. **23**, 8539–8546 (2023).
[37] X. Xue, M. Chen, Y. Luo, T. Qin, X. Tang, and Q. Hao, Light Sci Appl **12**, 2 (2023).
[38] G. Myeong, W. Shin, K. Sung, S. Kim, H. Lim, B. Kim, T. Jin, J. Park, T. Lee, M.S. Fuhrer, K. Watanabe, T. Taniguchi, F. Liu, and S. Cho, Nat Commun **13**, 4328 (2022).
[39] A. Jagtap, B. Martinez, N. Goubet, A. Chu, C. Livache, C. Gréboval, J. Ramade, D. Amelot, P. Trousset, A. Triboulin, S. Ithurria, M.G. Silly, B. Dubertret, and E. Lhuillier, ACS Photonics **5**, 4569–4576 (2018).
[40] T.H. Dang, A. Vasanelli, Y. Todorov, C. Sirtori, Y. Prado, A. Chu, C. Gréboval, A. Khalili, H. Cruguel, C. Delerue, G. Vincent, and E. Lhuillier, Nano Lett. **21**, 6671–6677 (2021).
[41] M. Chen, L. Lu, H. Yu, C. Li, and N. Zhao, Advanced Science **8**, 2101560 (2021).